This document is confidential and is proprietary to the American Chemical Society and its authors. Do not copy or disclose without written permission. If you have received this item in error, notify the sender and delete all copies.

Gold Nanostar Spatial Distribution Impacts the Surface-Enhanced Raman Scattering Detection of Uranyl on Amidoximated Polymers

Journal:	Langmuir	
Manuscript ID	la-2021-00132z.R1	
Manuscript Type:	Article	
Date Submitted by the Author:	n/a	
Complete List of Authors:	Phan, Hoa; The University of Iowa, Chemistry Vinson, Claire; University of Iowa, Chemistry; Smith College Haes, Amanda; University of Iowa, Chemistry	

SCHOLARONE™ Manuscripts

Gold Nanostar Spatial Distribution Impacts the
Surface-Enhanced Raman Scattering Detection of
Uranyl on Amidoximated Polymers

Hoa T. Phan, Claire Vinson, and Amanda J. Haes*

Department of Chemistry, University of Iowa, Iowa City, Iowa 52242, United States

ABSTRACT

The plasmonic properties of carboxylated gold nanostars distributed on amidoximated polyacrylonitrile (AO PAN) electrospun polymer films scale with surface-enhanced Raman scattering (SERS) intensities for coordinated uranium (VI) oxide (uranyl) species. This two-step plasmonic sensor first isolates uranyl from solution using functionalized polymers, then carboxylated gold nanostars are subsequently deposited for SERS. Spatially resolved localized surface plasmon resonance (LSPR) and SERS facilitate

correlated nanostar optical density and uranyl quantification. To reduce sampling bias, gold nanostars are deposited in an inverted drop coating geometry and measurements are conducted inside resulting nanoparticle coffee rings that form on the polymer substrates. This approach naturally preserves the plasmonic properties of gold nanostars while reducing the deposition of nanoparticle aggregates in active sensing regions thereby maximizing both the accuracy and precision of SERS measurements. Several advances are made. First, second derivative analysis of LSPR spectra facilitates the quantification of local nanostar density across large regions of the sensor substrate by reducing background variations caused by the polymeric and gold materials. Second, local nanostar densities ranging from 140-200 pM cm are shown to result in uranyl signals that are independent of nanostar concentration. Third, a Gibbs free energy of uranyl adsorption to carboxylated nanostars is estimated at 8.4±0.2 kcal/mol. Finally, a linear dynamic range of ~0.3 to 3.4 µg U/mg polymer is demonstrated. Signals vary by 10% or less. As such, the uniformity of plasmonic activity of distributed gold nanostars and the employment of spatially resolved spectroscopic measurements on the composite nanomaterial sensor interface facilitates the quantitative detection of uranyl while also reducing dependence on user expertise and selected sampling region. These important advances are critical for the development of a user-friendly SERS-based sensor for uranyl.

INTRODUCTION

Gold nanostars are a common substrate for the trace detection of small molecules using surface-enhanced Raman scattering (SERS) because of the large electric fields generated at their positive and negative curvature regions. 1-4 The optical properties of gold nanostars correlate to SERS and are often monitored using localized surface plasmon resonance (LSPR) spectroscopy. 2, 5-7 The electric fields that extend from the nanostar surfaces arise from the LSPR, which leads to electromagnetically enhanced Raman signals for molecules in these fields. 8-9 LSPR spectral features vary with nanoparticle composition, 10-12 shape, 2, 10 and size, 13-14 so SERS enhancements also depend on these same parameters. In addition to solution-phase measurements, gold nanostars have been deposited onto polymers, 15-16 glass, 17 and paper 18-19 for sensor development, but

surface roughness and chemistry of these substrates often influence the optical properties^{16, 19} and spatial distribution¹⁷⁻¹⁸ of gold nanostars thereby limiting quantitative molecular detection.

Herein, detection of uranium (VI) oxide (uranyl) is targeted because it is a common water-soluble uranium species that adversely impacts human health with chronic exposure.²⁰ Resultantly, the US EPA established that 30 µg/L of uranium (U) is the maximum allowable concentration for safe drinking water.²⁰ Many regions throughout the US, including those in the southwest, regularly have drinking water with U concentrations that exceed this limit. Detection methods that are sensitive, facilitate low detection limits and quantitative responses, and provide information related to speciation are key to reducing public risk. Normal Raman and SERS can be used for this purpose.²¹ The symmetric stretch associated with the pentagua uranyl complex is well-known and centered at ~870±1 cm⁻¹ in normal Raman,²² a value that red-shifts upon coordination to other ligands. Raman detection, however, is limited by the inherent uranyl cross section, and as a result, only concentrations down to mM are easily

detectable. To improve detection limits, SERS can be employed for uranyl detection down to EPA limits.^{2, 12, 16, 23-27} In most cases, the plasmonic nanostructures used for SERS are functionalized with carboxylate,^{2, 12, 16, 23-24} phosphonate,²⁵ azo,²⁶ or amide²⁷ groups to facilitate detection. For instance, carboxylated gold nanostars successfully facilitated SERS detection of uranyl in solution down to 0.12 μM (i.e. ~28 μg U/L).²⁰ This detection limit depends on many factors including the LSPR properties of the SERS substrates used^{2, 28} as well as the SERS focal volume.^{2, 29} As such, reproducible uranyl quantification depends on the optical density of the plasmonic nanostructures in the probe volume.^{2, 12, 24-25, 30}

Previously, we demonstrated that uranyl detection and quantification are possible in various sample matrices using amidoximated polyacrylonitrile (AO PAN) electrospun polymers and carboxylated gold nanostars. ¹⁶ Because the AO PAN polymers successfully isolated uranyl from solution before SERS-active substrates were introduced to the sensor, sample matrix effects were minimized. Only polymer regions that contained uniform densities of gold nanostars and appeared similar under the

microscope were sampled. This is important because drop coating plasmonic nanoparticles onto a substrate often leads to the formation of a coffee ring that contain high densities of nanoparticles. 16-17 Large but varying SERS signals were observed on the coffee rings. To minimize signal variations arising from plasmonic fluctuations at coffee ring interiors, an inverted drop coating geometry was developed for a similar indirect SERS detection platform. 17 In this geometry, a nanoparticle droplet was applied to the substrate so that nanoparticle aggregates formed at the droplet center rather than its edges. These aggregates could either be pipetted away or naturally deposited on the coffee ring to minimize their influence on SERS measurements.

Herein, spatially resolved LSPR and SERS microscopies are used simultaneously to assess and minimize plasmonic variations of carboxylated gold nanostars on AO PAN for quantitative uranyl detection. Novel to this study, the spatial distribution and electromagnetic properties of gold nanostars deposited on the polymer are locally quantified using LSPR microscopy mapping and second derivative LSPR spectral analysis. As a result, spectral complexity arising from background variations are

eliminated thus enabling quantification of local nanostar density. Next, uranyl intensities are shown to be insensitive to local nanostar densities that range from 140 to 200 pM·cm. This important finding provides a non-biased guideline for selecting sensing regions for uranyl detection on electrospun polymer films. Quantification down to 0.3 µg U/mg polymer is demonstrated. By considering interactions between gold nanostars, the polymer substrate, and uranyl and correlating spatially resolved spectral measurements at an interface, realization of a user-friendly sensor for uranyl detection that minimizes sampling bias is possible.

MATERIALS AND METHODS

Materials. Gold(III) chloride trihydrate (HAuCl₄·3H₂O), 4-(2-hydroxyethyl)1-piperazine propanesulfonic acid (EPPS), and 6-mercaptohexanoic acid (MHA) were purchased from Sigma Aldrich. Sodium hydroxide (NaOH), hydrochloric acid (HCl), nitric acid (HNO₃), and ethanol were purchased from Fisher Scientific. Ultrapure water (18.2 $M\Omega$ ·cm⁻¹) was obtained from a Barnstead Nanopure System (Dubuque, IA). All

glassware were cleaned with aqua regia (3:1 HCl/HNO₃) and rinsed with ultrapure water before drying in the oven. A stock solution of U(VI) (Flinn Scientific) was prepared to a final concentration of 1.208 mM UO₂²⁺ (aq) from UO₂(NO₃)₂·6H₂O(s) in water and was validated using liquid scintillation counting (LSC). CAUTION: (UO₂)(NO₃)₂·6H₂O contains radioactive ²³⁸U, which is an alpha emitter and like all radioactive materials, must be handled with care. These experiments were conducted by trained personnel in a licensed research facility with special precautions taken towards the handling, monitoring, and disposing of radioactive materials.

Polymeric materials were fabricated, functionalized, and characterized following a previously published procedure (see SI).^{16, 31} To determine the morphology and diameter of the fibers, polymer substrates were coated with Au/Pd (Emitech Sputter Coater K550) then imaged using a scanning electron microscope (SEM, Hitachi S-4800). Fiber diameter was analyzed using Image Pro using at least 100 measurements (N). Protocols for uranyl uptake and validation followed previously published protocols.¹⁶ Uranyl solutions with concentrations ranging from 1-10 μM were prepared by adding

known amounts of a 1000 mg/L depleted uranium (SPEX CertiPrep) stock solution into 10 mM HEPES buffer (pH = 6.8 adjusted using NaOH) then incubated with 5 mg of dehydrated AO PAN diced polymer samples for 18 hours. The polymer samples were then rinsed with DI water and dried in vacuum for an hour before usage. Non-amidoximated PAN polymers were used as controls. Triplicate samples were prepared for each uranyl concentration so that one sample could be used for LSC validation¹⁶ and the other two for SERS measurements. See SI for detailed information.

Gold Nanostar Synthesis, Functionalization, and Characterization. Gold nanostars were synthesized using a previously published protocol.⁶ First, a 60 mM EPPS solution was adjusted to a pH of 7.5 using 1 M NaOH solution. Next, 80 mL of 120 mM EPPS was stirred (520 RPM) in a 100 mL beaker for 5 minutes before 0.8 mL of 20 mM HAuCl₄ was quickly added to the EPPS solution. Stirring continued for 10 minutes then was stopped before the solution was equilibrated for 24 hours. The resulting nanostar solution was centrifuged (1800xg for 45 minutes) three times and sequentially dispersed

in 10 and 5 mM EPPS before being stored in a 5 mM EPPS solution until use or functionalization.

Au nanostars were functionalized using 20 mL aliquots of 1 nM gold nanostars (ε = 2.84 \times 10⁹ M⁻¹·cm⁻¹)³² in 5 mM EPPS (pH 7.50) that were stirred at 350 RPM. Next, 2 mL of 10 mM MHA in ethanol was added dropwise at a rate of 10 µL/minute. After 18 hours, the solution was centrifuged (1800xg for 40 minutes) thrice and washed with 1 mM NaOH before storage in 1 mM EPPS. Prior to deposition onto polymer substrates, functionalized gold (Au@MHA) nanostars were doubly centrifuged at 2000xg for 40 minutes to a concentration of 40 nM.

Nanostar structure was evaluated using transmission electron microscopy (TEM). A JEOL 1230 TEM equipped with a Gatan CCD camera and a 120 keV acceleration voltage was used. Samples were prepared by dispersing 10 µL of the nanostars (1:1 water:ethanol) onto 400 mesh copper grids coated with Formvar and carbon (Ted Pella). At least 100 Au nanostars were analyzed using Image Pro to evaluate the radius of curvature of

the nanostar tips and the overall average

dimensions. A representative image and

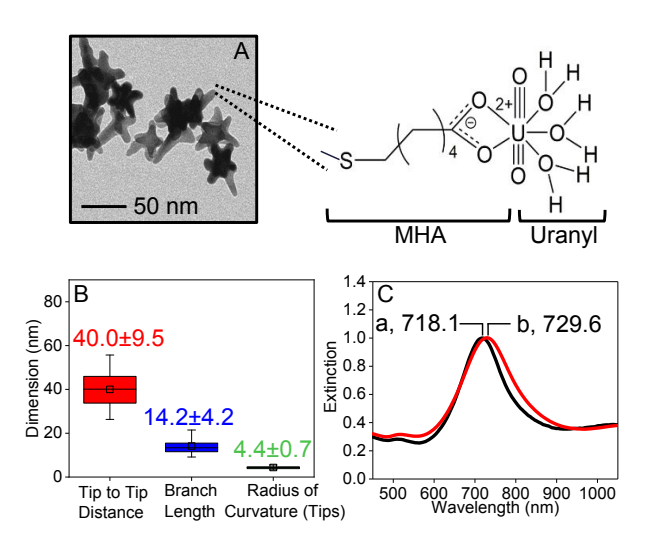


Figure 1. Structural and optical characterization of gold nanostars. (A) TEM of gold nanostars coordinated to and an example of uranyl coordinated to Au@MHA nanostars on the polymer. (B) TEM analysis of gold nanostar structure (N=1823). (C) Representative LSPR spectra of gold nanostars (a) before (718.1 nm) and (b) after (729.6 nm) MHA functionalization ($\Delta\lambda_{max}$ =11.5 nm).

size analysis of carboxylated nanostars are shown in Figures 1A and 1B, respectively.

LSPR Measurements and Analysis. A previously published protocol 16 was used for upright drop coating. Briefly, AO PAN polymers with and without uranyl were diced into 3 mm × 3 mm squares, and 1 µL droplets of 1 nM Au@MHA nanostars in 80% ethanol were pipetted onto polymer squares every 2 minute until 10 µL was deposited. For inverted drop coating, polymers (with and without uranyl) were diced into 5 mm discs, hydrated with ~2.5 µL water, and inserted into a holder so that a 4 mm cross section was visible. Aliquots of 1 µL 10 - 40 nM Au@MHA nanostars in water were deposited on the polymers in an inverted configuration¹⁷ where the polymer was placed in a support frame with the amidoximated side down and the nanostar solution was introduced from below using a perpendicularly oriented micropipette. The polymers were allowed to equilibrate for at least 30 minutes at 20 °C for both deposition geometries. Fiducial markers were used for registry of LSPR and SERS.

LSPR spectra of Au and Au@MHA nanostar solutions were collected in methacrylate cuvettes (path length = 1 cm) using an ultraviolet-visible (UV-vis) spectrometer (i-trometer BWTek) with a halogen lamp (Figure 1C). LSPR spectra of these same

materials deposited onto AO PAN were collected using a semi-homebuilt microscope (Olympus IX71) coupled to the same detector and light source. Sensor substrates were placed on a glass slide (PVDF side down) then hydrated using 30 μ L water and covered by a glass cover slip. A 20x objective lens was used to collect LSPR spectra (cross section = 400 μ m, integration time = 2 seconds, 10 averages). Raster scanning (500 μ m steps) facilitated the collection of LSPR spectral maps. Reference data were collected using hydrated AO PAN substrates that did not contain gold nanostars.

Nanostar density and electromagnetic coupling between nanostars were evaluated by integrating spectral areas from 480-570 nm and 670-785 nm, respectively. Second derivative extinction spectra were evaluated after smoothing using a second order polynomial and Savitzky-Golay protocol. This allowed the signal magnitude (maximum – minimum) to be determined, which was subsequently used for gold nanostar quantification.

SERS Measurements and Analysis. SERS measurements were collected using a semi-homebuilt Raman microscope (Olympus BX51) equipped with an ExamineR

Raman detector and fiber optic solid-state laser with an excitation wavelength (λ_{ex}) of 785 nm, which was operated at 15-16 mW. The laser was focused onto the sample through a 20x objective, so the laser spot diameter was 10 μ m. Data were collected using an integration time (t_{int}) of 30 seconds. Samples were hydrated using 50 μ L water, enclosed by a coverslip, and lightly pressed together before being placed on the microscope stage. Spectral maps were generated by raster scanning across the sample using 500 μ m steps. SERS signals arising from uranyl were quantified by integrating the spectra from 860-800 cm⁻¹.

RESULTS AND DISCUSSION

Evaluation of Au@MHA Nanostar Spatial Distribution on Electrospun Polymer

Substrates. SERS intensities depend on local analyte concentration as well as enhancements induced from chemical and electromagnetic effects associated with SERS.³³ Previously, nanoparticles were shown to readily aggregate forming a coffee

ring when drop coating was used.¹⁷ This leads to SERS signals that vary nonuniformly across a substrate¹⁷ and depend on the electromagnetic properties of the nanostructures instead of the molecular species.²⁹ To overcome this challenge, an inverted geometry¹⁷ is adopted to promote the uniform distribution of gold nanostars over much as the sensor substrate. This is

confirmed using LSPR microscopy and

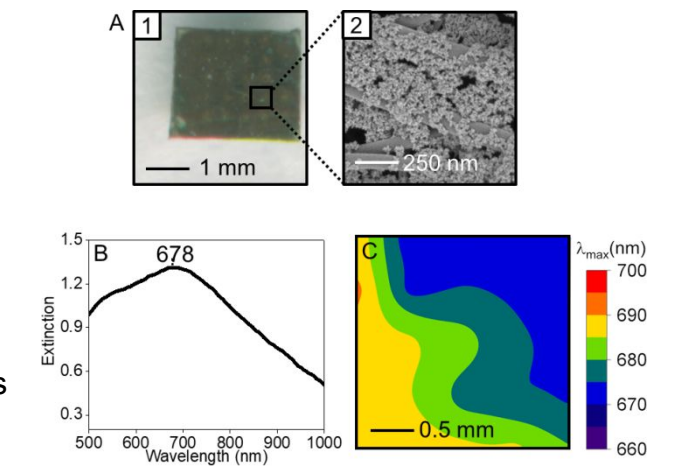


Figure 2. Gold nanostar distribution on a polymer sensor substrates using the traditional, upright drop-coating method. (A) (1) Photograph and (2) SEM image of Au@MHA nanostars deposited on the electrospun polymer. An (B) example LSPR spectrum and (C) spectral map associated with λ_{max} of deposited gold nanostars.

second derivative signal processing to quantify the spatial distribution and plasmonic properties of the plasmonic nanomaterials and to eliminate spectral background variations thus facilitating quantification of local nanostar density, respectively.

The distribution of gold nanostars deposited on electrospun AO PAN can be characterized using both microscopy and spectroscopy. For instance, a photograph and SEM image of a sub-region of the polymer coated with gold nanostars applied via traditional drop coating are shown in Figure 2A. These images indicate gold nanostars deposit in non-uniform, multilayers, a result consistent with our previously reported studies. 16 Here, we also demonstrate that the LSPR properties of the deposited nanostars exhibit a single broad resonance with a maximum wavelength (λ_{max}) centered at ~678 nm (Figure 2B), in contrast to the multiple resonance features centered at ~520 and ~720-730 nm observed for solution-phase nanostars.^{2, 6} Spectra of deposited gold nanostars are collected using an inverted optical microscope coupled to a white light source and CCD, then analyzed. This configuration is feasible given the polymeric sensor substrates are thin (less than ~120 µm) and do not absorb light at visible

wavelengths. The LSPR spectra for gold nanostars deposited on the polymer films do not correlate to the hybridized optical properties associated with Au nanostar core and branches. Instead, the broad feature observed is consistent with scattering, which arises from both gold nanostar multilayers and the electrospun polymer fibers. While the LSPR feature is broad, variations in this band can be quantified spatially by determining the full width at half maximum (Γ) via raster scanning the substrate. This value exhibits a median value of 267 nm and an average of 265.8±4.5 (2% RSD) over a 6.25 mm² sampling area. The extinction maximum wavelength (λ_{max}) associated with this same feature varies similarly as shown in Figure 2C. These data range from 670.6 to 691.5 nm (average = 680.0±7.2 nm, median = 677.8 nm).

To limit the impact of these optical variations and to promote a SERS signal that depends on analyte concentration, we build on a method first reported by Porter¹⁷ in which an inverted drop coating configuration was used for depositing nanostructures onto supporting substrates for indirect SERS detection. As shown in Figure 3A-1, this approach facilitates the formation of a natural coffee ring and minimizes the deposition

of aggregated nanostructures at the ring interior. SEM images collected on the ring

(Figure 3A-2) reveal densely packed, multilayers of nanostars while lower densities of

materials are deposited at interior areas (Figure 3A-3). Variations in nanostar density on

and inside the coffee ring cause differences in the optical properties that arise from the

nanostructures, properties that can be

spectrally observed using LSPR microscopy.

The inverted deposition geometry

preserves the original plasmonic

lineshape of gold nanostars when

sampled inside the coffee ring. LSPR

spectra are collected using the same

aforementioned inverted microscope

setup. Several important observations

are noted for spectra collected at the

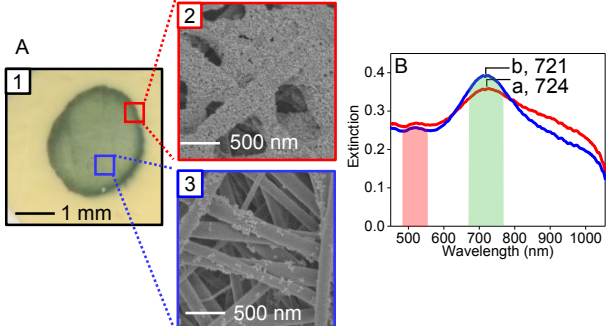


Figure 3. Gold nanostar distribution on the electrospun polymer substrates. (A) (1) Photograph and SEM images of Au@MHA nanostars located (2) on and (3) inside a coffee ring on a representative electrospun polymer substrate. (B) Corresponding LSPR spectra collected (a) on and (b) inside the coffee ring. Shaded regions are used for integrated determining ratios area associated with gold nanostar cores (480-570 nm) and branches (670-785 nm). Gold nanostars are deposited using an inverted drop-coating configuration.

interior of coffee rings. First, LSPR spectra collected from nanostars distributed on the polymeric substrates are similar to spectra collected in solution. Namely, two resonances, which are attributed to hybridized plasmon resonances associated with nanostar core and branches, are observed (Figure 3B).³⁴ Next, spectral line shapes and λ_{max} values suggest that minimal to no electromagnetic coupling is occurring between nanostructures at the interior of coffee rings while short range coupling effects are apparent³⁷ when measuring spectra from nanostars on coffee rings. As shown in Figure 3B, the λ_{max} associated with nanostar branches does not change significantly (~3 nm) but the Γ, which is determined from the baseline (i.e., the inflection point³⁸ near 565 nm), is narrower by ~23 nm when measured inside vs. on the coffee ring. Additionally, the magnitude of the signal associated with nanostar branches vs. cores (see highlighted flocculation areas in Figure 3B) are larger for nanostars deposited inside vs. on the ring. This

Table 1. LSPR spectral analysis of gold nanostars deposited using traditional and inverted drop coating

· · · · ·					
	المرت مرادا	las contro d			
	ı Obrianı	inverted			

		Inside Ring	On Ring
λ _{max} (nm)	680.0 ± 7.2	720.8 ± 0.8	722.8 ± 2.6
	(%RSD=1.1%)	(0.1%)	(0.4%)
Γ (nm)	265.8 ± 4.5	153.3 ± 1.9	176.0 ± 10.7
Branch/Core	Not Detected	1.68 ± 0.02	1.41 ± 0.05
Ratio		(1.4%)	(3.4%)

further supports that the optical properties arising from nanostars located on the ring

exhibit more electromagnetic coupling vs. those at interior regions.^{7, 16} As shown in

Table 1, statistical analysis of spatial measurements at these regions suggest the

plasmonic properties associated with nanostars are more uniform (i.e., smaller RSD)

and exhibit minimal electromagnetic coupling at the interior regions of the coffee rings.

Because the area inside a nanoparticle coffee ring was previously shown to exhibit uniform SERS signals for gold nanospheres containing extrinsic Raman labels, 17 a result observed directly for

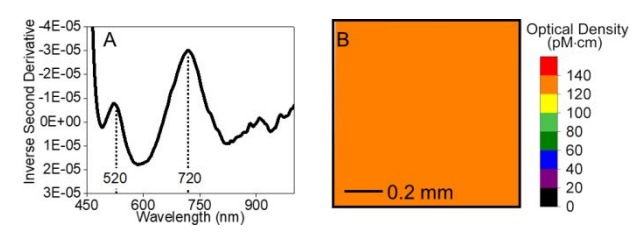


Figure 4. LSPR mapping using 30 nM gold nanostars deposited onto a polymer substrate using an inverted geometry. (A) Inverse second derivative LSPR spectra collected inside the coffee ring. (B) Representative LSPR map that quantifies local nanoparticle optical density inside the coffee ring on a polymer substrate. Experimental parameters: 20x objective and transmission geometry.

uranyl in Figure 4, the spatial distribution of gold nanostars in this same area is expected to be uniform. LSPR spectral imaging can be used to quantify variations in local

nanostar concentration across the polymeric substrate. Given the natural morphology and arrangement of the polymer fibers, spectral background fluctuates from spot to spot (see Figure S1). Scattering from both the polymer morphology and nanostars causes the LSPR spectral background to vary systematically at all wavelengths. This complicates determination of nanostar density using absolute extinction values.^{2, 32} To minimize these variations, second derivative processing of LSPR spectra are calculated. This process differentiates extinction values at consecutive wavelengths to eliminate systematic background variations while revealing plasmonic features of nanostars in raw LSPR data.³⁹⁻⁴⁰ An example of this analysis is shown in Figure 4A where inverse second derivative LSPR spectra are shown for gold nanostars that are uniformly distributed with minimal electromagnetic coupling. The two plasmonic features associated with gold nanostars are clearly observed around 520 and 720 nm, and the plasmonic feature near 720 nm can be used to compare local nanostar density across possible sensing regions.

To quantify gold nanostar concentration and local distribution, magnitude differences in second derivative extinction spectra are calculated from 600 to 700 nm using a modified form of Beer's law as follows:⁴¹

$$bC = \frac{ext_{2nd}}{\varepsilon_{2nd}}$$
 (eq. 1)

where \exp_{2nd} is the second-derivative extinction magnitude at the λ_{max} , ε_{2nd} is the second-derivative extinction coefficient (1.80 x 10⁵ M⁻¹), b is the optical path length, and C is the nanoparticle concentration. Because the optical path length depends on substrate thickness, which includes polymer, solvent, and gold nanostars, nanostar concentrations are reported as a product of path length and concentration; therefore, a metric that is proportional to local nanostar concentration on the polymeric materials is quantified.

A representative LSPR map inside the coffee ring is shown in Figure 4B where 1 µL of 30 nM Au@MHA nanostars is deposited on the polymeric substrate as previously described and evaluated. In this example, the Au@MHA nanostar optical density varies from 127 - 140 pM·cm (average =132 \pm 5 (4 % RSD), median = 131). Given this uniformity in gold nanostar distribution and plasmonic properties, SERS signals arising from uranyl are expected to be similarly

precise when sampled spatially. Of note,

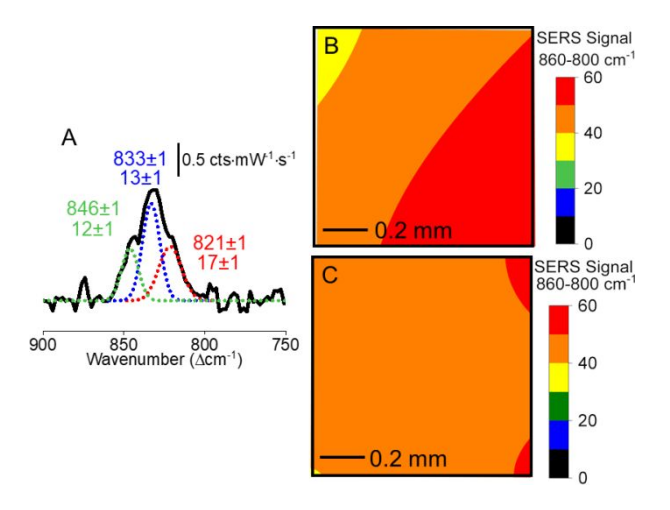


Figure 5. (A) Representative SERS spectra of 6.1 µg U/mg polymer collected inside the coffee ring. Representative spatial distribution of signal intensity (area) for uranyl on a 1x1 mm² area in the center of the polymer substrate upon (B) traditional and (C) inverted drop coating deposition SERS experimental geometries. parameters: λ_{ex} = 785 nm, P 15-16 mW, t_{int} = 30 sec. The laser was focused onto the sample through a 20x objective to a spot size of 10 µm. A 30 nM Au@MHA nanostar solution was deposited onto the hydrated polymers for SERS.

optical densities of nanostars deposited inside coffee rings are lower than those of nanostar multilayers deposited using the upright configuration (see Figure S2 for a

corresponding LSPR map). The high optical density arising from these multilayers lead to optical losses (scattering and plasmon damping⁴²) thus limiting the quantification of SERS signals.

Correlation between Nanostar Surface

Density and SERS Signals of Uranyl on

Functionalized Sensor Substrates. To

evaluate the SERS activity of uranyl from

Au@MHA nanostars deposited inside

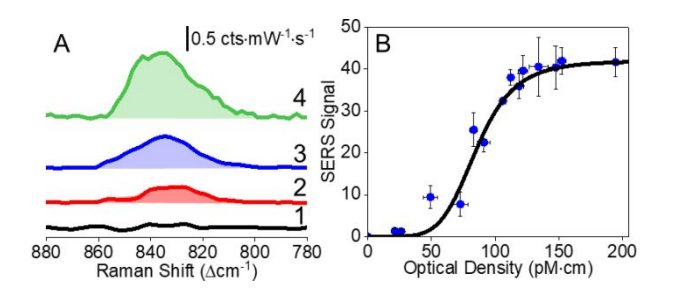


Figure 6. (A) Representative (1) normal Raman and SERS spectra collected on polymeric sensor substrates with nanostar densities of (2) 49±5, (3) 91±5, and (4) 195±6 pM·cm. Integrated areas associated with uranyl are shaded. (B) SERS signals associated with uranyl are plotted as a function of local nanostar density. Same experimental conditions as in Figure 5. Substrates containing 6.1 μg U/mg polymer were used. Gold nanostar concentration was varied from 0 – 40 nM to achieve varying nanostar quantities. Error bars represent standard deviations from at least three measurements.

coffee rings on amidoximated polymeric sensor substrates, SERS spectra are collected from ring interiors. This approach also minimizes signal variations caused by locally aggregated nanostructures. To do so, SERS spectra associated with uranyl is analyzed. Figure 5A shows a representative SERS spectrum where signals are well-above the

noise limit and reveal spectral signatures associated with uranyl. ^{2, 16} Upon spectral deconvolution, three vibrational features associated with uranyl are observed at 846±1 (Γ=12±1), 833±1 (13±1), and 821±1 (17±1 cm⁻¹) cm⁻¹. These are assigned as UO₂(bidentate-COO)⁺, UO₂(OH)(monodentate-COO), and (UO₂)₃(OH)₅(monodentate-COO)/UO₂(OH)(bi-COO), respectively. Assignments are based on ~13 and ~24 cm⁻¹ red-shifts for mono and bidentate carboxylate coordination geometries, respectively, ⁴³ and the most likely uranyl species that should be present in solution. A thorough discussion of this rationale is found in the SI and Figure S4. These vibrational modes are consistent with uranyl coordinated to carboxylate (MHA) on the nanostars as previously observed¹⁶ and described in Table S1.

The uniform nanostar optical densities found at coffee ring interiors lead to SERS signals for uranyl that are independent of sampling region. Relative uranyl signals are assessed by integrating the spectral envelope for all uranyl species. To compare signal variations on substrates prepared using our previous approach (upright droplet deposition) and an inverted geometry, representative SERS maps for uranyl are shown

in Figures 5B and 5C, respectively. SERS intensities for uranyl are generally small and close to noise for the traditional samples with an average S/N of 4.2±2.4. These SERS signals fluctuate from 37 - 63 (area (AU), average = 349±6 AU (12% RSD), median = 49 AU) while noise, which was calculated between 770-700 cm⁻¹, varies from 0.17 to 0.59 AU (24% RSD) and exhibits a median of 0.33 AU (Figure S3A). Across identical sampling areas, samples prepared using the inverted deposition geometry exhibit more uniform SERS signals (Figure 5C) and noise (Figure S3B). While signals range from 40-53 AU (10% RSD) and exhibit a median of 48 AU, the average and median noise values are 0.04±0.01 AU (12% RSD) and 0.04, respectively. This result is consistent with variations in plasmonic signals collected using spatially resolved LSPR measurements. Of note, noise is reduced in the new approach as scattering from nanostar aggregates and multilayers are minimized. Given the improvements in the S/N associated with SERS and homogeneity at the interior regions of coffee rings, only spectroscopic responses collected in these regions and with inverted drop coating geometries are considered moving forward.

For a given analyte concentration, SERS signals depend on the optical density of the plasmonic nanostructures.^{29, 37} To evaluate the impact of gold nanostar density on the SERS signal, samples containing 6.1 ± 1.1 µg U/mg polymer are used. Both LSPR and SERS spectra are collected spatially and correlated. Example normal Raman and SERS spectra in the uranyl window are shown in Figure 6A and contain nanostar densities ranging from 0 - 195 ± 6 pM·cm. Of note, the concentration of adsorbed uranyl on the polymer substrate is not sufficient for normal Raman spectroscopy thus emphasizing the importance of plasmonic nanoparticles and SERS detection.

In the presence of carboxylated gold nanostars, uranyl is easily observed; but SERS intensities for uranyl depend on nanostar density. As shown in Figure 6B, SERS intensities follow a sigmoidal response as a function of nanostar density. The Hill equation $(S_{SERS} = S_{SERS}^{max} \left(\frac{C_{nanostar}^n}{\kappa^{n-1}\xi^n + C_{nanostar}^n}\right))$, ⁴⁴⁻⁴⁶ is used to analyze these data. This suggests that each gold nanostar coordinates to ~6 uranyl species (n) with an intrinsic dissociation constant (ξ) of 10.7 and a multiplier characterizing the change in the affinity (κ) of 12.4. Because κ is larger than 1, positive cooperativity is indicated between uranyl

and carboxylated ligands on gold nanostars. 45 Below ~30 pM·cm nanostar optical densities, SERS signals for uranyl are not statistically different from noise. Increasing the nanostar optical density up to 140 pM·cm causes SERS signals to increase linearly. Between nanostar densities of 140 - 200 pM·cm, SERS signals do not vary significantly and are saturated. We attribute these effects to uniform electromagnetic enhancements³⁷ coupled with minimal optical loss.⁴⁷⁻⁴⁸ At these surface densities, SERS signals are likely arising from electric fields extending from positive and/or negative curvature features on the nanostars. As the number of gold nanostars increases in a given focal volume, slight enhancements from electromagnetic coupling between gold nanostars increase while optical losses (reabsorption and damping) also become more apparent. An approximately stable signal is observed until losses dominate thereby causing the signal to degrade in magnitude. As such, SERS signals collected from sensor locations with nanostar densities ranging from 140-200 pM·cm are used in subsequent experiments because these regions exhibit plasmon independent SERS responses for uranyl.

Uranyl Quantification using the Sensor. Now that an approach to collect SERS signals that are independent of local nanostar density is established, the impact of uranyl uptake is evaluated. First, U uptake is varied from 0 to 6.1 ± 1.1 μg U/mg polymer (determined using LSC). Next, carboxylated nanostars are deposited on the polymer until a nanostar surface density between 140 - 200 pM·cm is obtained. Finally, correlated SERS spectra are collected across the same areas to quantify uranyl signal.

Figures 7A and 7B show representative spatially resolved nanostar densities from LSPR and uranyl concentrations from SERS, respectively. In this sample, localized gold nanostar densities vary by 156±10 pM·cm (6% RSD), and uranyl signals exhibit an average of 39±3 AU (9% RSD, median = 39 AU). Low and similar relative standard deviations in these values collected across analyzed regions suggest highly correlated spectral signals where gold nanostars are uniformly deposited, that is, without impacts from particle aggregation.

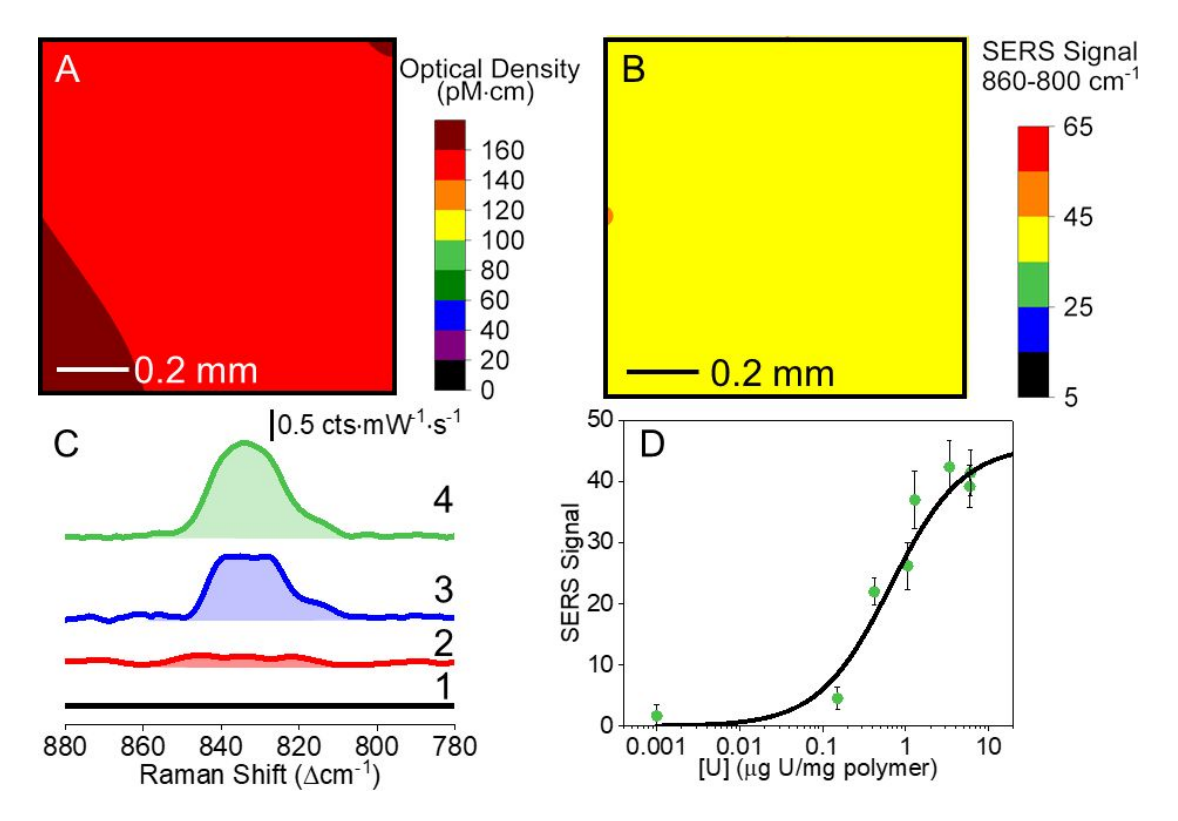


Figure 7. Representative spectral maps associated with spatially registered (A) nanostar optical density and (B) SERS signal for uranyl on an amidoximated polymer substrate. Data are reported inside coffee rings only. The polymer contains 5.96 μg U/mg polymer. (C) Representative averaged SERS spectra collected using the sensor (1) 0, (2) 0.2, (3) 0.4, and (4) 6.1 μg U/mg polymer (integrated areas associated with uranyl are highlighted). Gold nanostar densities ranged from 140-200 pM·cm. (D) SERS signals for uranyl are plotted as a function of U uptake/mg polymer. Same experimental conditions as in Figure 5. Error bars represent standard deviations from at least three measurements.

As uranyl uptake increases from 0 to 6.1 µg U/mg polymer, the uranyl signal observed

in SERS also increases as shown in Figure 7C. The demonstrated limit of detection is

near the EPA limit. The data follow the Langmuir adsorption isotherm model⁴⁹ ($S_{SERS} =$ $S_{SERS}^{max}\left(\frac{K_{eq} \cdot C_{Uranyl}}{1 + K_{eq} \cdot C_{Uranyl}}\right)$ Eq. 2) as a function of uranyl concentration (C_{uranyl}) as shown in Figure 7D. The resulting equilibrium constant (K_{eq}) and Gibbs free energy associated with uranyl-carboxylate coordination, which is calculated from K_{eq} using the following equation: $\Delta G = -RT \ln(K_{eq})$ (Eq. 3), are 1.51±0.44 (µg U/mg polymer)⁻¹ and 8.42±0.17 kcal/mol, respectively, consistent with previous reports.² This systematic response reveals a linear dynamic range from ~0.3 to 3.4 µg U/mg polymer. This quantitative, detectable range is reasonable as it is below ~8.8 µg U/mg polymer.³¹ which was previously demonstrated to be the maximum U uptake capacity of these AO PAN polymers. Uranyl uptake capacity by these materials is limited by diffusion/mass transfer and surface area, and SERS signals are limited by the focal volume sampled.⁵⁰ Further variations in uranyl uptake, polymer surface area to volume ratio, and optics used for SERS could be considered for tuning this linear dynamic range to expand the utility of the response for this quantitative SERS sensor.

CONCLUSIONS

In summary, correlated spatially resolved LSPR and SERS microscopies resulted in the quantitative detection of uranyl to environmentally relevant uranyl concentrations on electrospun AO PAN substrates. This approach reduced impacts of signal fluctuations arising from the natural heterogeneity in material morphology and gold nanostar deposition. Several materials and measurement advances were demonstrated. First, local gold nanostar concentration on the polymeric sensor substrates was determined through second derivative analysis using spatially resolved LSPR microscopy, which eliminated spectral background variations and facilitated signal quantification. Second, depositing the nanostars in an inverted geometry improved the uniformity in nanostar spatial distribution and optical densities that were sampled. Impacts of deposited aggregates were minimized as a result. Third, when local nanostar density was 140+ pM·cm, uranyl signals were Langmuir-like. Consequently, a Gibbs free energy associated with uranyl-carboxylate interactions was quantified as 8.4±0.2 kcal/mol. Finally, a linear dynamic range of uranyl detection extended from ~0.3 to 3.4 µg U/mg polymer. This quantitative range was achieved across the sensor substrate and varied

by less than 10% for all samples. This improvement in materials understanding and sampling demonstrated for the SERS detection of uranyl is an important step toward the development of a user-friendly sensor for uranyl.

SUPPORTING INFORMATION.

The supporting information is available free of charge. Fabrication, functionalization, and characterization of electrospun polymers; uranyl uptake and validation; spot to spot analysis of LSPR spectra; LSPR map of traditional, upright nanostar deposition, SERS noise variations on the polymer sensors, and vibrational mode assignments for uranyl species.

AUTHOR INFORMATION

Corresponding Author*

Amanda J. Haes – Department of Chemistry, University of Iowa, Iowa City, Iowa 52242, United States; orcid.org/0000-0001-7232-6825; Phone: (319) 384-3695. Fax (319) 335-1270. E-mail: amanda-haes@uiowa.edu.

Authors

Hoa T. Phan – Department of Chemistry, University of Iowa, Iowa City, Iowa 52242 United States; orcid.org/0000-0002-0793-8822; Claire Vinson – Department of Chemistry, Smith College, Northampton, Massachusetts 01063 and Department of Chemistry, University of Iowa, Iowa City, Iowa 52242 United States; clairevinsn@gmail.com

Author Contributions

The manuscript was written through contributions of all authors. All authors have given approval to the final version of the manuscript. The authors declare no competing financial interest.

ACKNOWLEDGEMENT

Research reported in this publication was supported by the National Institute of Environmental Health Sciences of the National Institutes of Health under Award Number R01ES027145. Hoa T. Phan thanks the University of Iowa for the Ballard and Seashore dissertation fellowship. Claire Vinson acknowledges the National Science Foundation grant NSF-1757548 for the summer research experience for undergraduate (REU)

program at the University of Iowa. This research was facilitated by the IR/D (Individual Research and Development) program associated with AJH's appointment at the National Science Foundation. We thank Prof. David Cwiertny and his group members for fabricating and characterizing the polymer fiber materials both before and after uranyl uptake.

REFERENCES

- 1. Meng, X.; Dyer, J.; Huo, Y.; Jiang, C., Greater SERS Activity of Ligand-Stabilized Gold Nanostars with Sharp Branches. *Langmuir* **2020**, *36* (13), 3558-3564.
- 2. Lu, G.; Forbes, T. Z.; Haes, A. J., SERS Detection of Uranyl Using Functionalized Gold Nanostars Promoted by Nanoparticle Shape and Size. *Analyst* **2016**, *141* (17), 5137-5143.
- 3. D'Hollander, A.; Mathieu, E.; Jans, H.; Vande Velde, G.; Stakenborg, T.; Van Dorpe, P.; Himmelreich, U.; Lagae, L., Development of Nanostars As A Biocompatible Tumor Contrast Agent: Toward in Vivo SERS Imaging. *Int. J. Nanomedicine* **2016**, *11*, 3703-3714.
- 4. Saverot, S.; Geng, X.; Leng, W.; Vikesland, P. J.; Grove, T. Z.; Bickford, L. R., Facile, Tunable, and SERS-Enhanced HEPES Gold Nanostars. *RSC Advances* **2016**, *6* (35), 29669-29673.
- 5. Xi, W.; Haes, A. J., Elucidation of HEPES Affinity to and Structure on Gold Nanostars. *J. Am. Chem. Soc.* **2019**, *141* (9), 4034-4042.

- 6. Chandra, K.; Culver, K. S. B.; Werner, S. E.; Lee, R. C.; Odom, T. W., Manipulating the Anisotropic Structure of Gold Nanostars using Good's Buffers. *Chem. Mater.* **2016**, *28* (18), 6763-6769.
- 7. Khoury, C. G.; Vo-Dinh, T., Gold Nanostars For Surface-Enhanced Raman Scattering: Synthesis, Characterization and Optimization. *J. Phys. Chem. C* **2008**, *112* (48), 18849-18859.
- 8. Willets, K. A.; Van Duyne, R. P., Localized Surface Plasmon Resonance Spectroscopy and Sensing. *Annu. Rev. Phys. Chem.* **2007**, *58*, 267-297.
- 9. Campbell, D. J.; Xia, Y., Plasmons: Why Should We Care? *J. Chem. Educ.* **2006**, *84* (1), 91-96.
- 10. Shrestha, K. B.; Haes, J. A., Improving Surface Enhanced Raman Signal Reproducibility Using Gold-coated Silver Nanospheres Encapsulated in Silica Membranes. *J. Opt* **2015**, *17* (11), 114017.
- 11. Pierre, M. C. S.; Haes, A. J., Purification Implications on SERS Activity of Silica Coated Gold Nanospheres. *Anal. Chem.* **2012**, *84* (18), 7906-7911.
- 12. Jiang, J.; Wang, S.; Deng, H.; H., W.; J., C.; Liao, J., Rapid and Sensitive Detection of Uranyl Ion with Citrate-Stabilized Silver Nanoparticles by the Surface-Enhanced Raman Scattering Technique. *Royal Soc. Open Sci.* **2018**, *5* (11), 181099.
- 13. Phan, H. T.; Heiderscheit, T. S.; Haes, A. J., Understanding Time-Dependent Surface-Enhanced Raman Scattering from Gold Nanosphere Aggregates using Collision Theory. *J. Phys. Chem. C* **2020**, *124* (26), 14287-14296.
- 14. Harder, R. A.; Wijenayaka, L. A.; Phan, H. T.; Haes, A. J., Tuning Gold Nanostar Morphology for the SERS Detection of Uranyl. *J. Raman Spectrosc.* **2021**, *52* (2), 497-505.
 - 15. Yilmaz, H.; Pekdemir, S.; Ipekci, H. H.; Kiremitler, N. B.; Hancer, M.; Onses, M. S.,

Ambient, Rapid and Facile Deposition of Polymer Brushes For Immobilization of Plasmonic Nanoparticles. *Appl. Surf. Sci.* **2016**, *385*, 299-307.

- 16. Lu, G.; Johns, A. J.; Neupane, B.; Phan, H. T.; Cwiertny, D. M.; Forbes, T. Z.; Haes, A. J., Matrix-Independent Surface-Enhanced Raman Scattering Detection of Uranyl Using Electrospun Amidoximated Polyacrylonitrile Mats and Gold Nanostars. *Anal. Chem.* **2018**, *90* (11), 6766-6772.
- 17. Crawford, A. C.; Young, C. C.; Porter, M. D., Gold Nanoparticle Labels and Heterogeneous Immunoassays: The Case for the Inverted Substrate. *Anal. Chem.* **2018**, *90* (14), 8665-8672.
- 18. Oliveira, M. J.; Quaresma, P.; Peixoto de Almeida, M.; Araújo, A.; Pereira, E.; Fortunato, E.; Martins, R.; Franco, R.; Águas, H., Office Paper Decorated with Silver Nanostars An Alternative Cost Effective Platform For Trace Analyte Detection by SERS. *Sci. Rep.* **2017**, *7*(1), 2480.
- 19. He, S.; Chua, J.; Tan, E. K. M.; Kah, J. C. Y., Optimizing the SERS Enhancement of a Facile Gold Nanostar Immobilized Paper-Based SERS Substrate. *RSC Advances* **2017**, *7*(27), 16264-16272.
 - 20. U.S. Environmental Protection Agency. Pacific Southwest, Region 9, 2015.
- 21. Lu, G.; Haes, A. J.; Forbes, T. Z., Detection and Identification of Solids, Surfaces, and Solutions of Uranium Using Vibrational Spectroscopy. *Coord. Chem. Rev.* **2018**, *374*, 314-344.
- 22. Gál, M.; Goggin, P. L.; Mink, J., Mid-, Far-Infrared and Raman Spectra of Uranyl Complexes in Aqueous Solutions. *J. Mol. Struct.* **1984,** *114*, 459-462.
- 23. Trujillo, M. J.; Camden, J. P., Utilizing Molecular Hyperpolarizability for Trace Analysis: a Surface-Enhanced Hyper-Raman Scattering Study of Uranyl Ion. *ACS Omega* **2018**, *3* (6), 6660-6664.

- 24. Trujillo, M. J.; Jenkins, D. M.; Bradshaw, J. A.; Camden, J. P., Surface-Enhanced Raman Scattering of Uranyl in Aqueous Samples: Implications for Nuclear Forensics and Groundwater Testing. *Anal. Methods* **2017**, *9* (10), 1575-1579.
- 25. Ruan, C.; Luo, W.; Wang, W.; Gu, B., Surface-Enhanced Raman Spectroscopy for Uranium Detection and Analysis in Environmental Samples. *Anal. Chim. Acta* **2007**, *605* (1), 80-86.
- 26. Burneau, A.; Teiten, B., Surface-Enhanced Raman Spectra of Both Uranyl(VI) and 2-(5-Bromo-2-Pyridylazo)-5-Diethylaminophenol in Silver Colloids. *Vib. Spectrosc.* **1999**, *21* (1), 97-109.
- 27. Teiten, B.; Burneau, A., Detection and Sorption Study of Dioxouranium(VI) Ions On n-(2-Mercaptopropionyl)Glycine-Modified Silver Colloid by Surface-Enhanced Raman Scattering. *J. Raman Spectrosc.* **1997**, *28* (11), 879-884.
- 28. Schatz, G. C.; Van Duyne, R. P., Electromagnetic Mechanism of Surface-Enhanced Spectroscopy. In *Handbook of Vibrational Spectroscopy*, John Wiley & Sons, Ltd: Chichester, 2006; pp 759-774.
- 29. Pierre, M. C. S.; Mackie, P. M.; Roca, M.; Haes, A. J., Correlating Molecular Surface Coverage and Solution-Phase Nanoparticle Concentration to Surface-Enhanced Raman Scattering Intensities. *J. Phys. Chem. C* **2011**, *115* (38), 18511-18517.
- 30. Jiang, J.; Ma, L.; Chen, J.; Zhang, P.; Wu, H.; Zhang, Z.; Wang, S.; Yun, W.; Li, Y.; Jia, J.; Liao, J., SERS Detection and Characterization of Uranyl Ion Sorption On silver Nanorods Wrapped with Al₂O₃ Layers. *Microchim. Acta* **2017**, *184* (8), 2775-2782.
- 31. Johns, A.; Qian, J.; Carolan, M. E.; Shaikh, N.; Peroutka, A.; Seeger, A.; Cerrato, J. M.; Forbes, T. Z.; Cwiertny, D. M., Functionalized Electrospun Polymer Nanofibers for Treatment of Water Contaminated with Uranium. *Environ. Sci.: Water Res. Technol.* **2020**, *6* (3), 622-634.

- 32. de Puig, H.; Tam, J. O.; Yen, C.-W.; Gehrke, L.; Hamad-Schifferli, K., Extinction Coefficient of Gold Nanostars. *J. Phys. Chem. C* **2015**, *119* (30), 17408-17415.
- 33. Maher, R., SERS Hot Spots. In *Raman Spectroscopy for Nanomaterials Characterization*, Kumar, C. S. R., Ed. Springer-Verlag Berlin Heidelberg: Germany, 2012; pp 215-260.
- 34. Hao, F.; Nehl, C. L.; Hafner, J. H.; Nordlander, P., Plasmon Resonances of a Gold Nanostar. *Nano Lett.* **2007**, *7*(3), 729-732.
- 35. Raghavan, V.; Gupta, M.; Xiao, Z.; Gi Chae, H.; Liu, T.; Kumar, S., Investigation of Polyacrylonitrile Solution Inhomogeneity by Dynamic Light Scattering. *Polymer Engineering & Science* **2015**, *55* (6), 1403-1407.
- 36. Li, B.; Pan, S.; Yuan, H.; Zhang, Y., Optical and Mechanical Anisotropies of Aligned Electrospun Nanofibers Reinforced Transparent PMMA Nanocomposites. *Composites Part A: Applied Science and Manufacturing* **2016**, *90*, 380-389.
- 37. Solís, D. M.; Taboada, J. M.; Obelleiro, F.; Liz-Marzán, L. M.; García de Abajo, F. J., Optimization of Nanoparticle-Based SERS Substrates through Large-Scale Realistic Simulations. *ACS Photonics* **2017**, *4* (2), 329-337.
- 38. Muri, H. I.; Hjelme, D. R., LSPR Coupling and Distribution of Interparticle Distances between Nanoparticles in Hydrogel on Optical Fiber End Face. *Sensors* **2017**, *17* (12), 2723.
- 39. Karpinska, J., Basic Principles and Analytical Application of Derivative Spectrophotometry, Macro To Nano Spectroscopy. In *Macro to Nano Spectroscopy*, Uddin, J., Ed. IntechOpen: 2012.
- 40. Giese, A. T.; French, C. S., The Analysis of Overlapping Spectral Absorption Bands by Derivative Spectrophotometry. *Appl. Spectrosc.* **1955,** *9* (2), 78-96.
 - 41. Balestrieri, C.; Colonna, G.; Giovane, A.; Irace, G.; Servillo, L., Second-Derivative

Spectroscopy of Proteins. Eur. J. Biochem. 1978, 90 (3), 433-440.

- 42. Foerster, B.; Spata, V. A.; Carter, E. A.; Sönnichsen, C.; Link, S., Plasmon Damping Depends on the Chemical Nature of the Nanoparticle Interface. *Sci. Adv.* **2019**, *5*(3), eaav0704.
- 43. Quilès, F.; Burneau, A., Infrared and Raman Spectroscopic Study of Uranyl Complexes: Hydroxide and Acetate Derivatives in Aqueous Solution. *Vib. Spectrosc.* **1998,** *18*(1), 61-75.
- 44. Hill, A. V., The Combinations of Haemoglobin with Oxygen and with Carbon Monoxide. I. *Biochem. J.* **1913,** *7*(5), 471-480.
- 45. Juška, A., Minimal Models of Multi-Site Ligand-Binding Kinetics. *J. Theor. Biol.* **2008**, *255* (4), 396-403.
- 46. Buttersack, C., Modeling of Type IV and V Sigmoidal Adsorption Isotherms. *Phys. Chem. Chem. Phys.* **2019**, *21* (10), 5614-5626.
- 47. Zhang, Q.; Large, N.; Wang, H., Gold Nanoparticles with Tipped Surface Structures as Substrates for Single-Particle Surface-Enhanced Raman Spectroscopy: Concave Nanocubes, Nanotrisoctahedra, and Nanostars. *ACS Anal. Mater. Interfaces* **2014**, *6* (19), 17255-17267.
- 48. Jackson, J. B.; Westcott, S. L.; Hirsch, L. R.; West, J. L.; Halas, N. J., Controlling the Surface Enhanced Raman Effect Via the Nanoshell Geometry. *Appl. Phys. Lett.* **2003**, *82* (2), 257-259.
- 49. Haes, A. J.; Van Duyne, R. P., A Nanoscale Optical Biosensor: Sensitivity and Selectivity of an Approach Based on the Localized Surface Plasmon Resonance Spectroscopy of Triangular Silver Nanoparticles. *J. Am. Chem. Soc.* **2002**, *124* (35), 10596-10604.
 - 50. Langer, J.; Jimenez de Aberasturi, D.; Aizpurua, J.; Alvarez-Puebla, R. A.; Auguié,

B.; Baumberg, J. J.; Bazan, G. C.; Bell, S. E. J.; Boisen, A.; Brolo, A. G.; Choo, J.; Cialla-May, D.; Deckert, V.; Fabris, L.; Faulds, K.; García de Abajo, F. J.; Goodacre, R.; Graham, D.; Haes, A. J.; Haynes, C. L.; Huck, C.; Itoh, T.; Käll, M.; Kneipp, J.; Kotov, N. A.; Kuang, H.; Le Ru, E. C.; Lee, H. K.; Li, J.-F.; Ling, X. Y.; Maier, S. A.; Mayerhöfer, T.; Moskovits, M.; Murakoshi, K.; Nam, J.-M.; Nie, S.; Ozaki, Y.; Pastoriza-Santos, I.; Perez-Juste, J.; Popp, J.; Pucci, A.; Reich, S.; Ren, B.; Schatz, G. C.; Shegai, T.; Schlücker, S.; Tay, L.-L.; Thomas, K. G.; Tian, Z.-Q.; Van Duyne, R. P.; Vo-Dinh, T.; Wang, Y.; Willets, K. A.; Xu, C.; Xu, H.; Xu, Y.; Yamamoto, Y. S.; Zhao, B.; Liz-Marzán, L. M., Present and Future of Surface-Enhanced Raman Scattering. *ACS Nano* 2020, *14* (1), 28-117.

TOC Graphic

